Title

Accelerated wound healing by injectable microporous gel scaffolds assembled from annealed building blocks

Journal

Nature Materials, 14(7)

ISSN

1476-1122

Authors

Griffin, Donald R
Weaver, Westbrook M
Scumpia, Philip O
et al.

Publication Date

2015-07-01

DOI

10.1038/nmat4294

Peer reviewed

Published in final edited form as:

Nat Mater. 2015 July ; 14(7): 737–744. doi:10.1038/nmat4294.

Accelerated wound healing by injectable microporous gel scaffolds assembled from annealed building blocks

Donald R. Griffin[*], **Westbrook M. Weaver**[*], **Philip Scumpia**, **Dino Di Carlo**[**], and **Tatiana Segura**[**]

Summary

Injectable hydrogels can provide a scaffold for *in situ* tissue regrowth and regeneration, however these injected materials require gel degradation prior to tissue reformation limiting their ability to provide physical support. We have created a new class of injectable biomaterial that circumvents this challenge by providing an interconnected microporous network for simultaneous tissue reformation and material degradation. We assemble monodisperse micro-gel building blocks into an interconnected microporous annealed particle (MAP) scaffold. Through microfluidic formation, we tailor the chemical and physical properties of the building blocks, providing downstream control of the physical and chemical properties of the assembled MAP scaffold. *In vitro*, cells incorporated during MAP scaffold formation proliferated and formed extensive 3D networks within 48 hours. *In vivo*, the injectable MAP scaffold facilitated cell migration resulting in rapid cutaneous tissue regeneration and tissue structure formation within 5 days. The combination of microporosity and injectability achieved with MAP scaffolds will enable novel routes to tissue regeneration *in vivo* and tissue creation *de novo*.

The evolution of injectable materials for regenerative medicine has been driven by the need to recapitulate natural tissue function with a minimally invasive implantation procedure[1–3]. Optimization of these materials has been focused on tuning their bulk properties to regulate cell behavior through material stiffness[4] and chemical moieties, such as oligopeptides and growth factors[2,5]. Ultimately, these approaches are limited by physical constraints, as host cells must remodel this precisely tuned matrix in order to infiltrate and fully integrate with the material.

Successful materials for tissue regeneration must precisely match the rate of material degradation to tissue development. If degradation occurs too quickly then insufficient scaffolding will remain to support tissue ingrowth, while a rate that is too slow will prevent proper tissue development and can promote fibrosis[6]. Tuning of degradation rates based on

Correspondence and requests for materials should be addressed to tsegura@ucla.edu and/or dicarlo@ucla.edu.
*both authors contributed equally
**co-corresponding

Author Contributions: DRG and WMW contributed equally to this manuscript both in conceptual design, troubleshooting, experimental execution, and manuscript writing. PS performed Day 1 immunological analysis and *in vivo* interpretation. DD and TS contributed equally to overseeing experimental design and interpretation.

The authors claim no competing financial interests.

Supplementary Information is linked to the online version of the paper at www.nature.com/nature.

local environment has been approached using hydrolytically and enzymatically degradable materials[7,8], however, decoupling cellular infiltration with decreases in material mechanical stability has proven extremely challenging[1]. Promotion of cellular infiltration into the material can be approached using a lightly crosslinked matrix, however this often results in mechanical mismatch with surrounding tissues and poor material stability[9]. Alternatively, the hydrogel degradation rate can be tuned by altering the polymeric backbone identity[10] or crosslinking density[11], matching the rates of degradation and tissue formation. Although these techniques address specific limitations of injectable hydrogels, they do not provide a robust pathway to achieve bulk tissue integration that does not rely on prior material degradation.

Every wound site is unique in its physical and chemical requirements for functional tissue regeneration, requiring a material strategy that is robust to a variety of challenging degradation environments. We have created a new class of injectable biomaterials, Microporous Annealed Particle (MAP) gels that circumvent the need for material degradation prior to tissue ingrowth by providing a stably linked interconnected network of micropores for cell migration and bulk integration with surrounding tissue. Inspired by the success of microporous scaffolds generated *ex situ* (through the use of porogens[12–15]) that promote cell migration, we designed an injectable biomaterial that also possesses these interconnected networks by using a porogen-free, building block approach to scaffold formation. Our strategy to achieve these favorable features relies on the self-assembly of highly monodisperse hydrogel microparticle (μgel) building blocks formed by microfluidic water-in-oil droplet segmentation[16–18] (Fig. 1a). Lattices of μgel building blocks are then annealed to one another via surface functionalities to form an interconnected microporous scaffold either with or without cells present in the interconnected pores (Fig 1b,c). Microparticles have been used successfully for cellular encapsulation[19] and assembly[20,21] *in vitro*, as well as neural cell-coated delivery vehicles *in vivo*[22–24], however they have not been explored as covalently linked three-dimensional scaffolding for tissue regeneration. Further, the MAP scaffold can be injected and molded to any shape (Fig. 1d), providing a mechanically stable scaffold of interconnected microporous networks for cell ingrowth (Fig. 1e).

By combining injectability and microporosity, we have provided a novel biomaterial scaffold for efficient cellular network formation *in vitro* and bulk tissue integration *in vivo*. Our modular material also provides mechanical support for rapid cell migration, molecular cues to direct cell adhesion, and resorption after tissue regeneration. Through microfluidic fabrication, we precisely tailor the chemical and physical properties of the building blocks, allowing for downstream control of the properties of the emergent MAP scaffolds. Our novel building block-based approach in which robustly achieved *imperfect* self-assembly is desirable to achieve microporosity fundamentally changes the use and implementation of hydrogels as tissue mimetic constructs, providing a philosophical change in the approach to injectable scaffolding for bulk tissue integration.

From building blocks to porous scaffolds: μgel properties determine MAP scaffold characteristics

We used a microfluidic water-in-oil emulsion approach[16–18] to segment a continuous pre-gel aqueous phase into uniform scaffold building blocks[19] (Fig. 1a, Extended Data Fig. 1a–c). Generating μgel building blocks serially at the microscale, rather than using the typical vortex and sonication-based approaches[25,26], allowed tight control over the formation environment and ultimate material properties of the emergent MAP gel. By tuning the flow rates of both the pre-gel solution and the pinching oil flow, as well as the geometry of the microfluidic channel, we created a range of μgel sizes with low polydispersity (Fig. 2a–c). Although our fabrication method was serial, it retained practicality in its high throughput nature, with generation rates that ranged from 250 Hz for larger particles (>100 μm) to ~1200 Hz for small particles (~15 μm). This translated to roughly 100 μl of pre-swollen gel every 50 min for a single device. This approach ultimately resulted in particles that were highly monodisperse, both physically and chemically. Microfluidic generation of MAP building blocks is a readily scalable process: a practical requirement for wide adoption and use[27,28].

The resultant μgel building blocks were composed of a completely synthetic hydrogel mesh of multi-armed poly(ethylene)glycol-vinyl sulfone (PEG-VS) backbones decorated with cell-adhesive peptide (RGD) and two previously utilized transglutaminase peptide substrates[29–31] (K and Q). The μgels were crosslinked via Michael type addition with cysteine-terminated matrix metalloprotease-sensitive peptide sequences that allowed for cell-controlled material degradation and subsequent resorption.

The μgel building blocks were purified into an aqueous solution of isotonic cell culture media for storage. The μgel building blocks were annealed to one another to form a MAP gel via a non-canonical amide linkage between the K and Q peptides mediated by activated Factor XIII (FXIIIa), a naturally occurring enzyme responsible for stabilizing blood clots[30,32]. This enzyme-mediated annealing process, allowed incorporation of living cells into a dynamically forming MAP scaffold that contained interconnected microporous networks. Following addition of FXIIIa, but prior to scaffold annealing, a slurry of the μgel building blocks can be delivered via syringe application, ultimately solidifying in the shape of the cavity in which they are injected (Fig.1d,e). Structural changes leading to over a three-fold increase in storage modulus in the annealed gels was observed upon addition of FXIIIa to the μgel building blocks (Fig. 2d). We confirmed μgel annealing was necessary for scaffold formation via high-vacuum SEM observation, wherein upon dehydration the scaffolds adopted a highly stretched but interconnected mesh whereas building blocks without FXIIIa separated into individual spherical beads (Extended Data Fig. 2d,e).

By tuning the μgel building block size and composition we were able to generate a diverse set of assembled MAP scaffolds. By using building block sizes from 30 to 150 μm in diameter, we achieved networks with median pores diameters ranging from ~10 to ~35 μm (Fig. 2e,f). We also screened different PEG weight percentages and crosslinker stoichiometries to demonstrate a range of easily achievable building block storage moduli from ~10 to 1000 Pa (Extended Data Fig. 2a–c) that spans the stiffness regime necessary for

mammalian soft tissue mimetics[33–37]. Physically matched MAP and non-porous gels demonstrated differential degradation kinetics when exposed to a protease cocktail *in vitro*, indicating greater access of the protease to MMP-cleavable sites within the MAP gel due to its microscale porosity (Extended Data Fig. 2D).

MAP scaffolds facilitate cellular proliferation and three dimensional network formation *in vitro*

In order to assess the ability of the MAP scaffold to support cell growth and network formation, we developed an *in vitro* cell morphology and proliferation model using three human cell lines: Dermal Fibroblasts (HDF), Adipose-derived Mesenchymal Stem Cells (AhMSC), and Bone Marrow-derived Mesenchymal Stem Cells (BMhMSC). We dynamically incorporated a single-cell suspension within a FXIIIa annealed MAP gel. The three cell lines exhibited high cell viability (≥ 93%, Fig. 3b) following 24 hours of culture within the MAP scaffold. The HDF and AhMSC cell lines demonstrated continued proliferation over a six-day culture period with doubling times of 1.5 and 2 days, respectively (Fig. 3d). BMhMSCs were observed to undergo proliferation as well, however with an extended calculated doubling time of ~12 days.

Cells incorporated into the MAP scaffold began to exhibit spread morphology 90 minutes following the onset of annealing (Fig 3c, Extended Data Fig. 3 and 4). After 2 days in culture, all observed cells within the MAP scaffolds exhibited a completely spread morphology, which continued through day 6. Importantly, we observed extensive network formation for all cell lines by day 2. Cell networks increased in size and complexity through the entirety of the experiment. The BMhMSCs were of particular note, as their expansive network formation and slower proliferation rate indicated that these cells were able to spread to extreme lengths, forming highly interconnected cellular networks within the microporous scaffolds. Notably, cells that were grown in non-porous gels of identical chemical properties (5 wt%, G'=600 Pa gel, Fig. 3c) or mechanical properties (4.5 wt%, G'=350 Pa gel, Fig. 3c) maintained viability, but did not exhibit any appreciable network formation, even after six days in culture (Extended Data Fig. 4).

Injectable MAP scaffolds enable seamless tissue integration and normal tissue architecture *in vivo*

We hypothesized that the ability of the MAP scaffolds to enable both cell proliferation and expedient network formation *in vitro* was indicative of an ability to support *in vivo* cell migration and bulk tissue integration within the scaffold. To test our hypothesis, we utilized a murine skin wound healing model[38], addressing a tissue of interest for previous implanted porous biomaterials[39–41]. Wound contraction, critical for skin healing in loose-skinned mammals including mice, was prevented using a sutured rubber splint. This technique allows for healing through re-epithelialization and granulation, better simulating healing response of humans and fixed-skinned mammals[38,42]. Because of the injectability of the MAP scaffold, we were able to deliver the μgel building blocks directly to the wound site, followed by *in situ* annealing via exogenous FXIIIa (activated in the wound bed by

exogenous thrombin). This provided a seamless interface by simultaneously linking MAP building blocks to one another as well as to endogenous lysine and glutamine residues present in the surrounding tissue (Fig. 4a, top). Similarly, a seamless interface was observed for the chemically identical, nonporous bi-lateral control (Fig. 4a, bottom). Despite their similar interface, the MAP scaffold resulted in significantly faster wound closure than the non-porous controls (60% versus 100% remaining wound area after 5 days, respectively) when injected into the wounds of hairless (CLR:SKH1-*Hr*^{hr}) mice (Fig. 4b,c).

Accelerated wound closure mediated by the MAP scaffold was also observed in a longer wound healing experiment performed in BALB/c mice. After 7 days *in vivo*, the MAP scaffold lead to 39% wound closure, significantly greater than the no treatment control that allowed only 19% and the physically-matched nonporous control that allowed 7%. Non-annealing μgels, which lacked K and Q peptides, were unable to facilitate increased wound closure (only 10%) compared to the no treatment control. This indicates that the annealing process is critical to support faster wound closure, which is not due to the presence of μgels in the wound bed alone. Microporous gels created using a porogen-based casting method also showed an increased wound healing (27%) compared to a no treatment control, further supporting the hypothesis that microscale porosity enhances wound healing *in vivo*.

The disparities in wound closure rates led us to investigate the differences in tissue responses to the non-porous and MAP injectable gel. MAP scaffold injection resulted in extensive wound re-epithelialization after 5 days *in vivo*. We observed keratin-5^{+} cells with stratified squamous morphology (Fig. 5a, bottom panel, green) over the surface of the MAP scaffold, however no cells (keratin-5^{+} or otherwise) were observed past the non-porous wound edge (Fig. 5a, top panel, green). Importantly, the MAP scaffold was able to sustain the formation of what appeared to be a developing hair follicle with adjoining sebaceous gland within the wound bed (Fig. 5a, inset) resembling the structure of these glands in the uninjured skin (Extended Data Fig. 7). Further, we observed other instances of large Keratin-5^{+} tissue structures within the MAP scaffold including tubular structures and epithelial invaginations (Extended Data Fig. 7). Expression of the epithelial markers Keratin-5, Keratin-14, and CD49f was observed in both normal epidermis (Extended Data Fig. 8) and the keratinocytes and newly-formed basement membrane of the regenerating epidermis overlying the MAP gel. As expected, staining of Keratin-5 and -14 in the regenerating epidermis extended beyond the basilar keratinocytes as expansion of staining beyond the basilar layer and into the stratifying epidermis, consistent with a hyperproliferative epidermis[43]. These data indicate normal epithelial regeneration over the wound beds treated with MAP gel. While beyond the scope of this manuscript, we hypothesize that together, these results are an indication of higher order collective migration (i.e. movement of multicellular clusters in concert) contributing to epidermal regeneration. Although cells were able to infiltrate the non-porous bi-lateral controls (as indicated by DAPI staining), no evidence of re-epithelialization or cutaneous tissue formation was found after 5 days *in vivo*.

Through further investigation, we found that the MAP scaffold promoted bulk integration via complex vascular network formation *in vivo*[44–47]. After 5 days, both endothelial cells (PECAM-1^{+}) and supporting pericytes (both NG2^{+} and PDGFRβ^{+})[48,49] (Fig. 5c) were

present within the MAP scaffold, while only single branches of endothelial cells without supporting pericytes were present in the non-porous bilateral controls (Fig. 5b). The presence of co-localized endothelial cells and pericytes was evidence of a developing vascular network[50]. To our knowledge, this is the first instance of early (<7 days) pericyte migration into a synthetic injectable material or implanted porous scaffold without the inclusion of exogenous growth factors[39,40,51,52].

While investigating the seamless interface provided by the injectable scaffolds we observed differences in both overall and immune cell quantities at day 1 within an area extending 75μm into the scaffold and 75μm into the tissue adjacent to the scaffold (extended data figure 6). H&E staining revealed that 1 day post-injection, the MAP scaffolds contained significantly higher numbers of leukocytes within the scaffold whereas the non-porous bi-lateral controls displayed aggregation of leukocytes at the skin edge near the interface of the wound and scaffold (Fig. 6a). This corroborated the greater ease of cell mobility previously observed in our *in vitro* network formation experiments (Fig. 3). Further, the MAP scaffold and its surrounding tissue contained a significantly lower number of leukocytes (determined by a dermatopathologist blinded to the identity of the experimental treatment using standard H&E) when compared to the non-porous bi-lateral control of the same mouse (Fig. 6b). Consistent with one-day old wounds, greater than 90% of the leukocytes infiltrating the skin tissue or the MAP scaffold were neutrophils, as evidenced by their polymorphonuclear characteristic and granular cytoplasm. These results indicated a lower apparent inflammatory response to the MAP scaffolds at Day 1 and are consistent with previous studies demonstrating porous scaffolds allow for better infiltration of inflammatory cells, while non-porous scaffolds result in a barrier to tissue healing and accumulation of inflammatory cells at the wound/scaffold interface[53,54]. After 5 days post-injection, lower fractions of cells staining positive for CD11b, a marker for cells of the myeloid lineage responsible for early tissue inflammation[55,56], were present both in the surrounding tissue and within the MAP scaffold relative to the non-porous controls (Fig. 6c,d), suggesting a sustained lower inflammatory response[57], in agreement with what has been observed in other micro-porous scaffolds that are cast *ex vivo* and implanted *in vivo*[12]. Combined, these results support a presently underexplored geometric component to immune stimulation from chemically-identical injectable biomaterials.

MAP scaffolds: a new modular biomaterial

MAP scaffolds represent a new class of injectable biomaterial that introduces microscale interconnected porosity through robustly achieved imperfect self-assembly and annealing of individual building blocks[20,21]. This approach allows control of micro- and hierarchical macro-scale properties through deterministic chemical composition and microfluidic particle generation. Both incorporated live cells and surrounding host tissue are able to immediately infiltrate the scaffold without the need for material degradation, a feat never before accomplished using injectable scaffolds.

In vivo, the injectable MAP building blocks completely filled the tissue void, providing a seamless boundary with the surrounding tissue. The interconnected microporosity of the resulting MAP scaffold promoted cellular migration at the wound site that resulted in greater

bulk integration with the surrounding tissue while eliciting a reduced host immune response, in comparison to an injectable non-porous control. Ultimately, wounds treated with the MAP gel led to faster wound healing than untreated wounds as well as wounds treated with mechanically-matched non-porous gels or non-annealing μgels. Precast, microporous gels also showed increased wound healing, illustrating the importance of interconnected micro-porous networks for wound healing. Our results indicate that the MAP gel can expand the applicability of micro-porous hydrogels through its injectable nature.

We present a fundamental change in the approach to bottom-up modular biomaterials by utilizing the negative space of lattice formation to promote the development of complex three-dimensional networks on time scales previously unseen using current hydrogel technologies. The “plug and play” nature of this microfluidically-generated building block strategy allows the incorporation of a wide range of already established materials (e.g. fibrin or hyaluronic acid), signals (e.g. growth factors), and cell populations (e.g. stem cells). Complex combinations of building blocks with deterministic chemical and physical properties may enable tissue regeneration in a range of distinct physiological niches (e.g. neural, cardiac, skin, etc.), where MAP scaffolds are tailored to each niche via their building block properties. The unique combination of microporosity, injectability, and modular assembly inherent to MAP scaffolds has the potential to alter the landscape of tissue regeneration *in vivo* and tissue creation *de novo*.

Extended Data

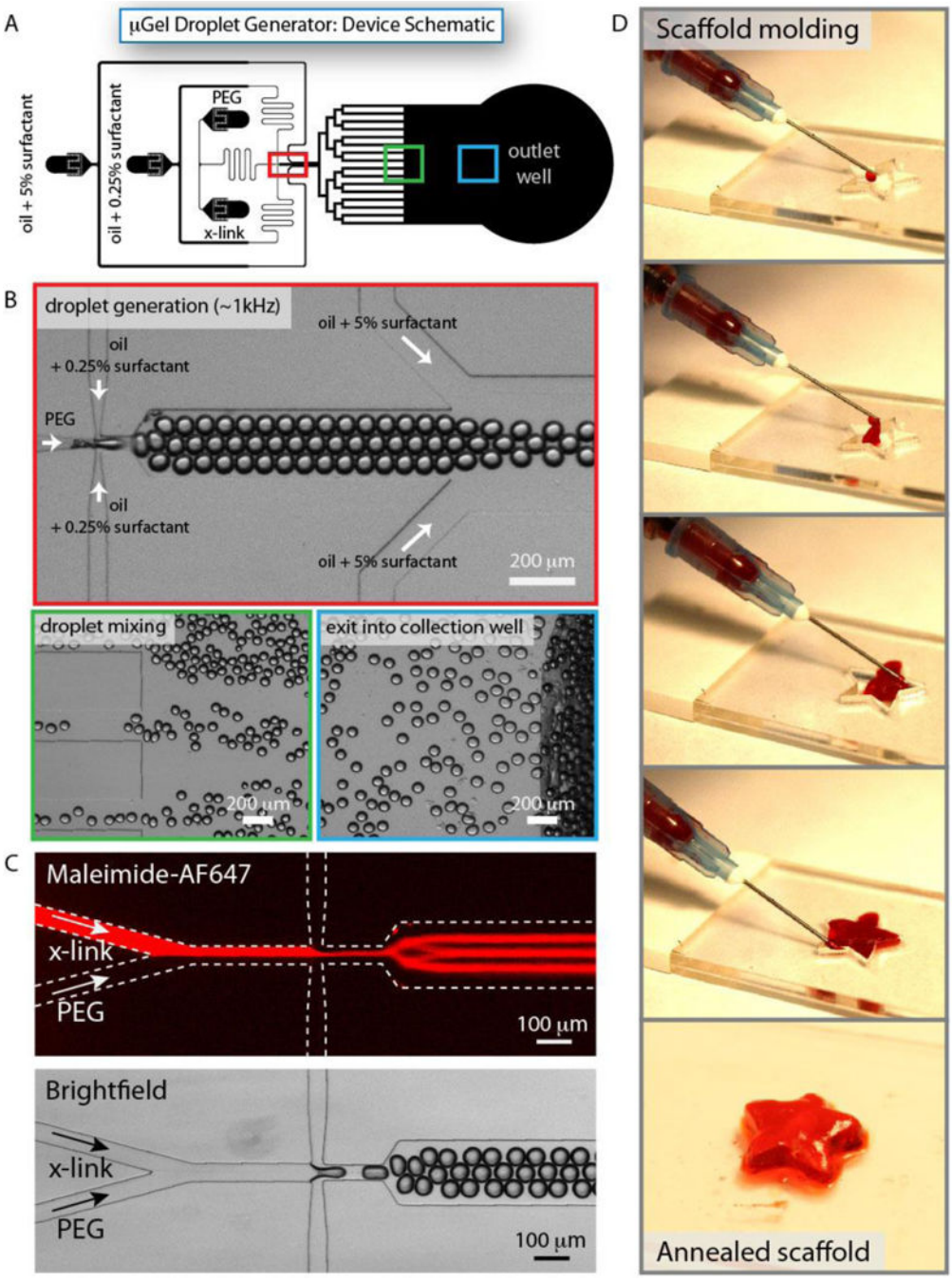

Extended Data Figure 1.

Microfluidic generation of building block µgels using a water-in-oil segmentation approach. A: Scheme of the microfluidic channel design used, with two aqueous inlets and two oil inlets. The collection well lies at the channel outlet (right side of scheme). B: In the droplet segmentation region, mineral oil with 0.25% Span 80 pinches and segments PEG pre-gel, and downstream a 5% Span 80 solution in mineral oil mixes and prevents downstream

coalescence of μgels before complete gelation. Droplet's internal contents mix during incubation in the bifurcation region and exit from the microchannel to the collection well. C High Peclet number (Pe > 10) prevents mixing of PEG and crosslinker (x-link) upstream of the segmentation region. D: Building block mixtures are injectable (e.g. 25 Gauge syringe) and can be molded to any shape (here shown after conforming to a star-shaped laser cut acrylic mold).

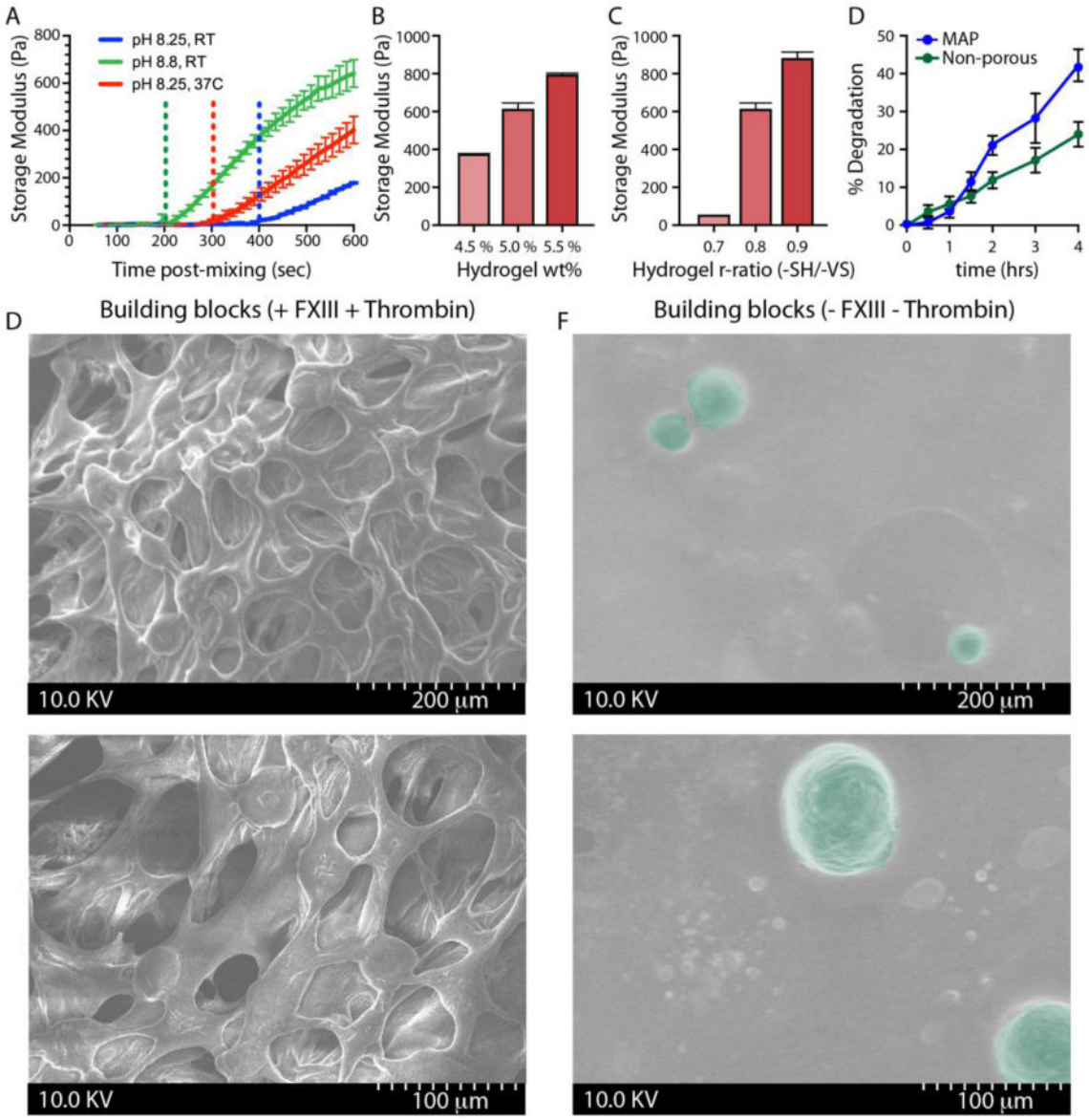

Extended Data Figure 2.

Control over the μgel building block parameters and the resultant MAP scaffolds. A: Gelation kinetics of the pre-polymer and crosslinker solution were altered by tuning solution pH and gelation temperature. The gelation environment chosen for this study was pH 8.25 and 37°C. Tuning both B: the weight % of PEG and C: the r-ratio of free crosslinker ends (-SH) to vinyl groups (-VS) on the PEG backbone allows control over the storage modulus of

the resultant gels. D: Degradation kinetics of MAP and non-porous (equal volumes) gels *in vitro*. MAP gels degrade faster than non-porous due to higher surface area to volume ratios and faster transport through the microporous gel. Degradation was carried out using 1:1000 TriplE, resulting in higher protease concentrations than in a wound bed and faster degradation kinetics. E: SEM images of a MAP scaffold annealed with FXIIIa. F: SEM images of μgel building blocks without FXIIIa. Green highlights indicate μgel building blocks.

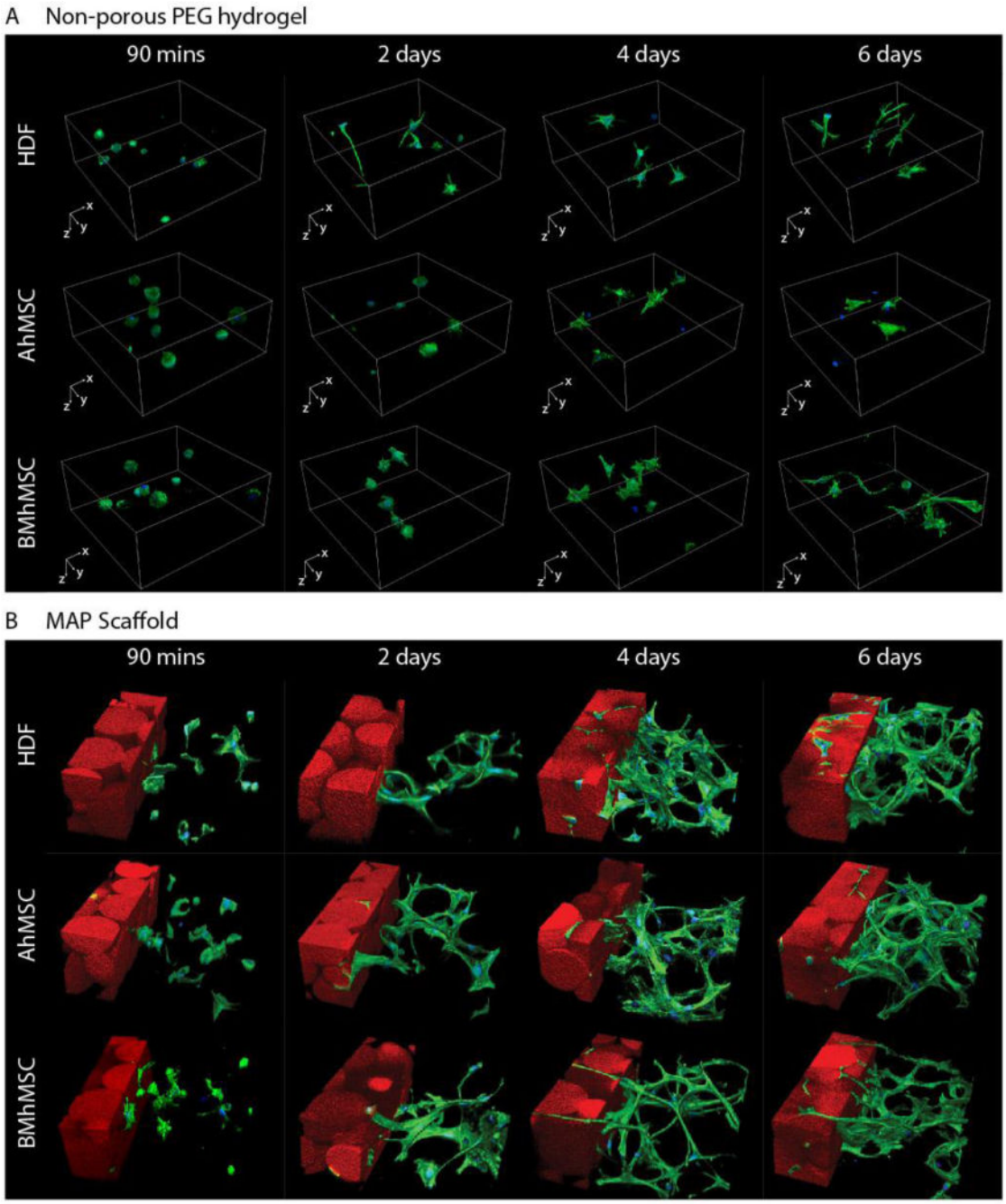

Extended Data Figure 3.

MAP scaffolds promote proliferation and network formation *in vitro*. A: representative images of HDF, AhMSC, and BMhMSC cell lines grown in non-porous PEG hydrogels of the same chemical composition as the MAP scaffolds. B: Representative images of the same cell lines grown in the MAP scaffolds.

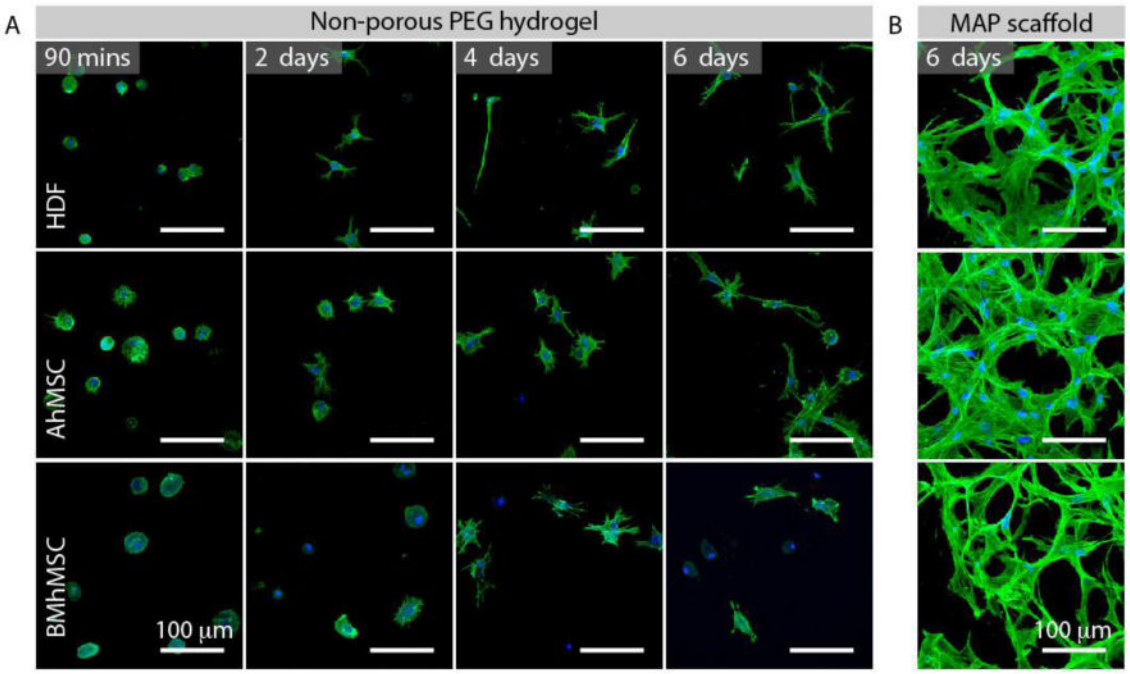

Extended Data Figure 4.

A: Maximum Intensity projections (MIPs) of the representative images from Extended Data Fig. 3a. B: MIPs of the MAP scaffolds after 6 days *in vitro* are shown for comparison.

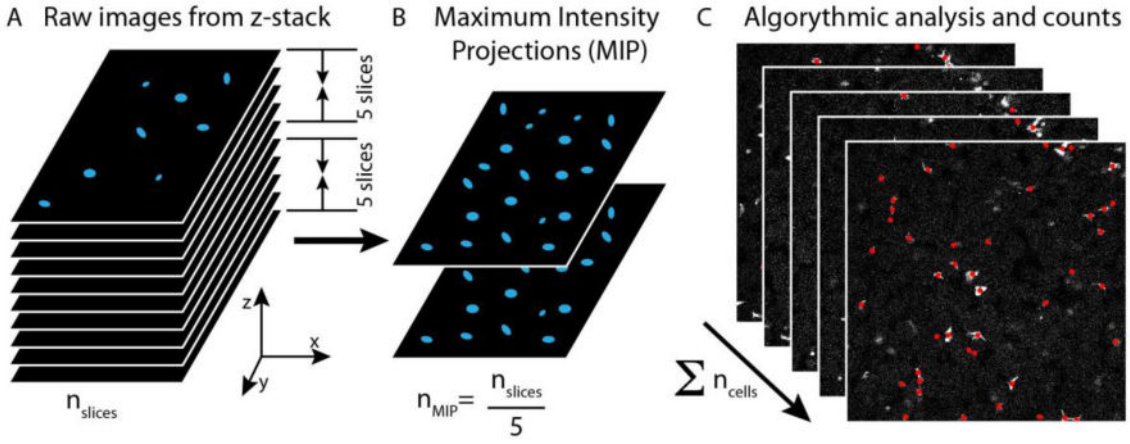

Extended Data Figure 5.

Scheme for image analysis of DAPI stained *in vitro* MAP gels for proliferation studies. A: Volumetric data within the scaffold is captured using a Nikon Ti eclipse confocal. Each volume is 317 × 317 × 150 um^3 (L × W × H), and consists of 55 slices. B: Slices are combined into 11 groups, each containing 5 slices. The maximum intensity projection (MIP)

of those five slices is projected into 1 2D image. C: These MIP images are then fed through an automated image analysis script written in MATLAB that filters the image, converts it to black and white, and counts the number of nuclei present in each section that is in focus, indicating that its centroid resides within the original five slices for that MIP. The counts for each MIP are summed for each gel, and this is presented as a total number of cells (plotted in figure 3d).

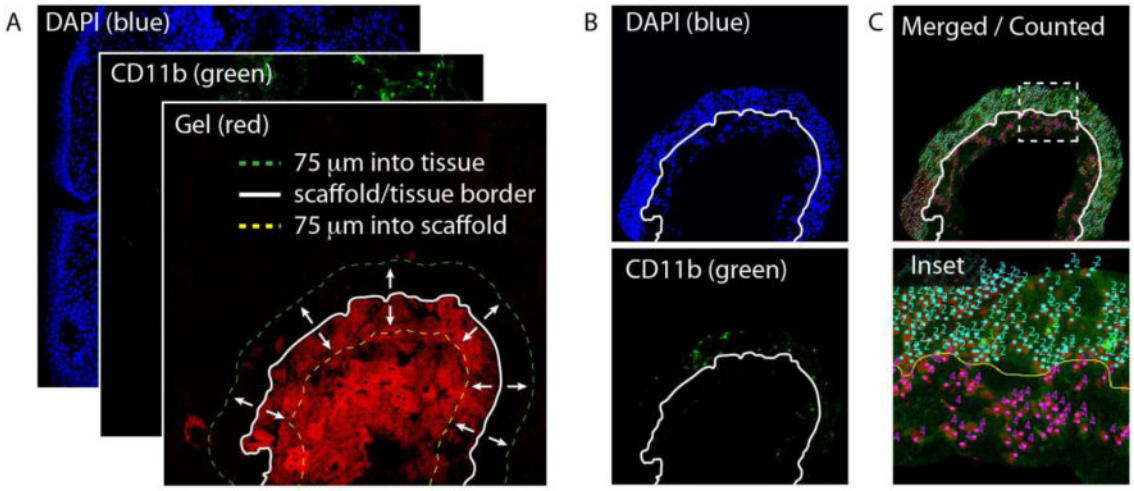

Extended Data Figure 6.

Scheme for technique used to analyze and quantitate the immune response of adjacent tissue to injected MAP scaffolds and non-porous bilateral controls 5 days post-injection. A: Each image is a 3×3 stitched image using a 40× water immersion objective (Nikon). These images are decomposed into their three distinct channels, where red represents injected gel, blue shows DAPI stained nuclei, and green indicated the presence of the CD11b antigen on cell surfaces, a marker of activated leukocytes. The red channel is used to find the edge of the gel-tissue interface, and this line is expanded 75μm both into the surrounding tissue and into the gel itself. B: These lines are then imposed on the green and blue channels, used as cropping margins. C: The resultant images are merged and counted, where data is presented as the fraction of DAPI nuclei associated with $CD11b^{+}$ signal. Three non-adjacent sections from each tissue block were used to count cells for both MAP scaffolds and non-porous controls.

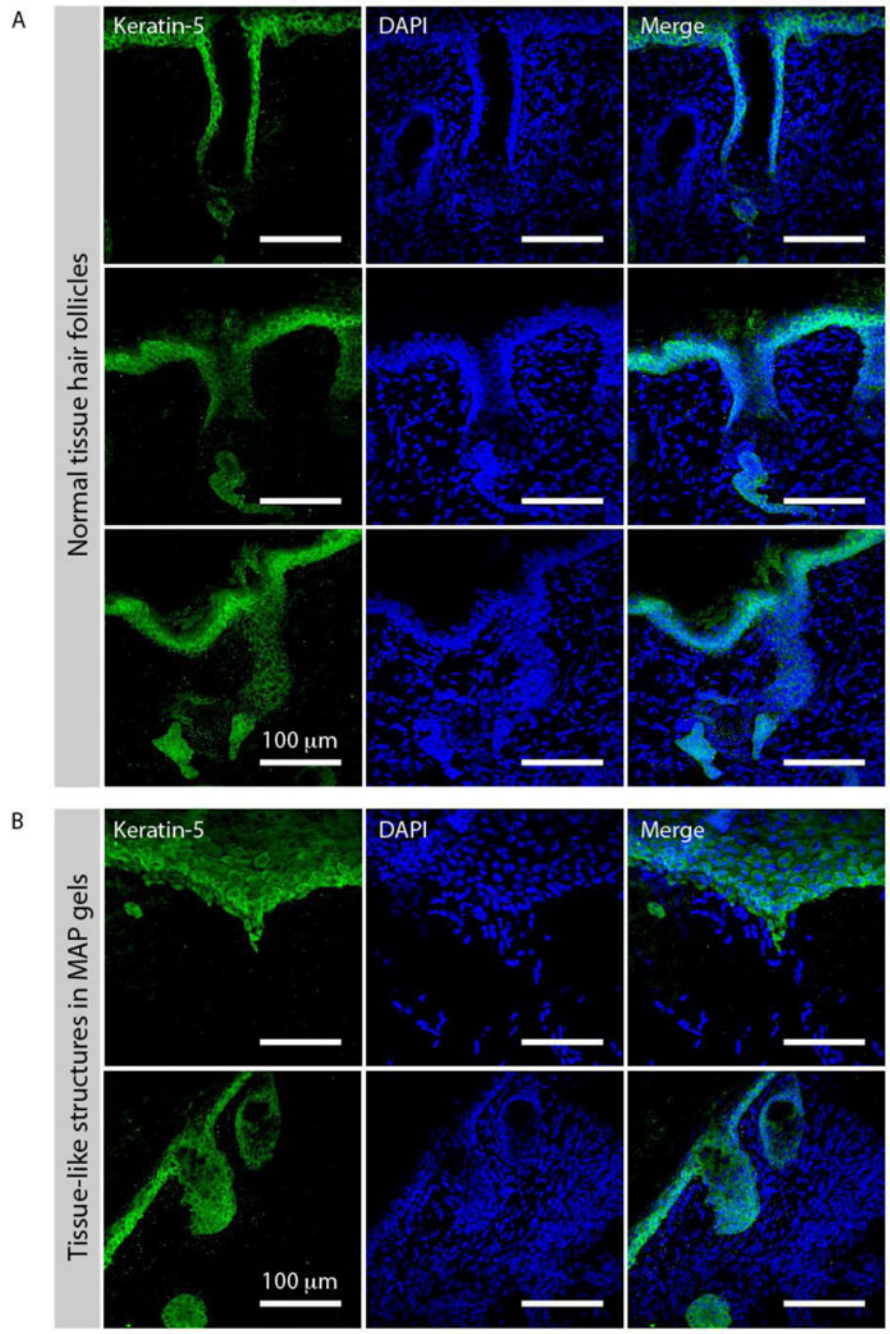

Extended Data Figure 7.

The MAP scaffold promotes tissue-like structure formation *in vivo*. A: Examples of normal hair follicles in non-wound areas of CLR:SKH1-*Hr*^{hr} mice. B: Two examples of structure formation within the MAP scaffold 5 days post injection. The early stages of large invaginations from the growing epidermis (top panel) and formation of structures (bottom panel).

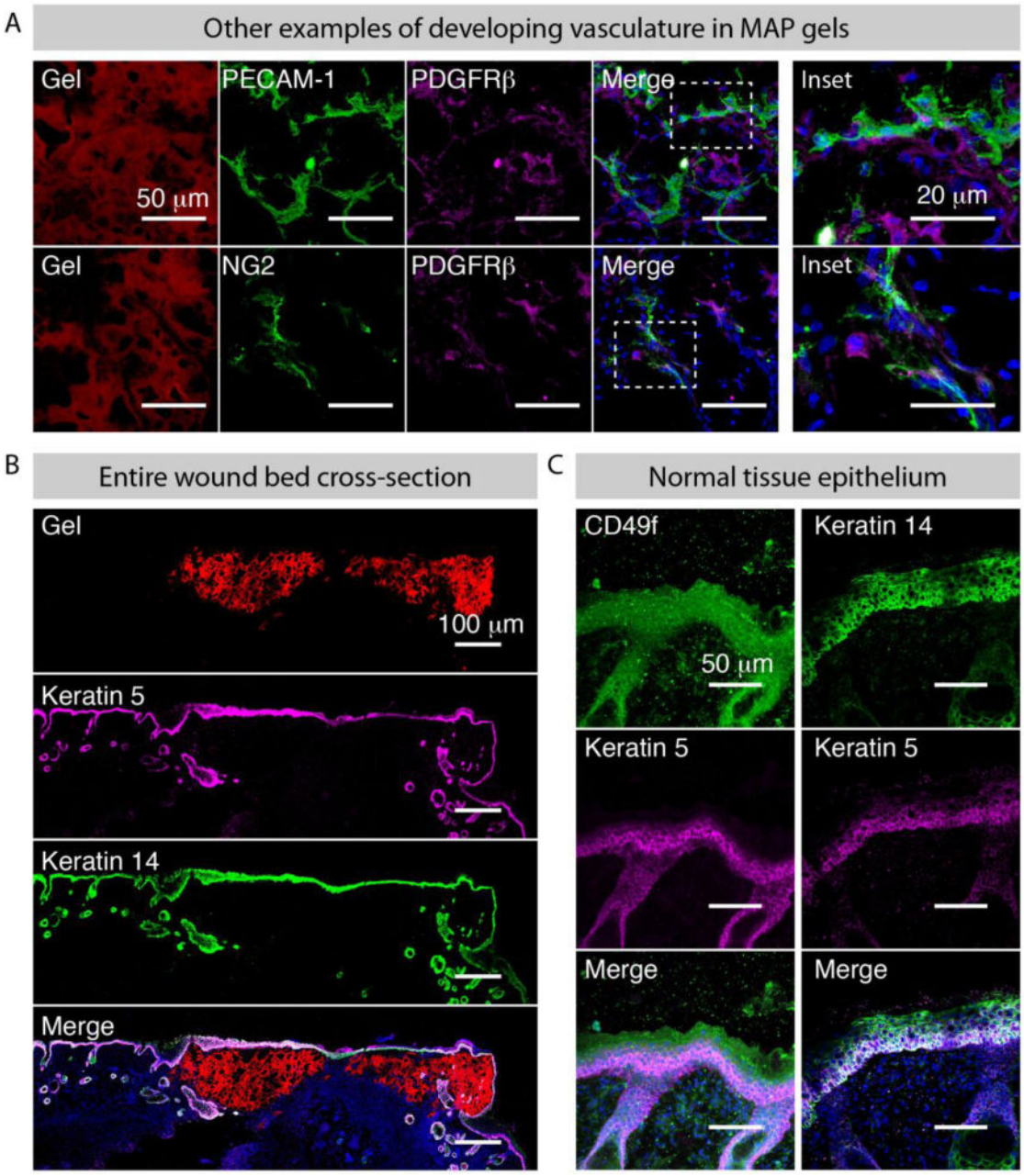

Extended Data Figure 8.

Large-scale tissue structures formed after treatment with the MAP scaffold *in vivo.* A: Further examples of vascular formation within the MAP scaffold after 5 days *in vivo*, as depicted via the juxtaposition of PECAM-1^{+} cells with PDGFRβ^{+} cells, as well as co-staining of NG2 and PDGFRβ on cells within the MAP scaffold. B: Stitched images of cross-sections of the wound beds treated with MAP after 5 days *in vivo*. These sections have been completely covered with sheets positive for both Keratin 5 and Keratin 14. C: Examples of normal tissue epithelial structure in the SKH1-*Hr*^{hr} mouse. Stratified epithelium is shown, where basilar layers express high levels of Keratin 5 and CD49f, where

as more apical layers continue to express Keratin -14, but loose Keratin 5 expression. This same pattern is seen in tissue growing within the wounds treated with MAP (figure 5).

Acknowledgments

The authors would like to thank Alan Vucetic for assistance with gelation kinetics measurements. This work was partially supported through the US National Institutes of Health Director's New Innovator Award (1DP2OD007113), NIH RO1HL110592, and the DermSTP Training Grant T32-AR058921.

References

1. Lee K, Hubbell JA. Tissue, cell and engineering. Curr Opin Biotechnol. 2013; 24:827–829. [PubMed: 24018131]
2. Guvendiren M, Burdick JA. Engineering synthetic hydrogel microenvironments to instruct stem cells. Curr Opin Biotechnol. 2013; 24:841–846. [PubMed: 23545441]
3. Discher DE, Mooney DJ, Zandstra PW. Growth Factors, Matrices, and Forces Combine and Control Stem Cells. Science. 2009; 324:1673–1677. [PubMed: 19556500]
4. Huebsch N, et al. Harnessing traction-mediated manipulation of the cell/matrix interface to control stem-cell fate. Nat Mater. 2010; 9:518–526. [PubMed: 20418863]
5. Wade RJ, Burdick JA. Engineering ECM signals into biomaterials. Mater Today. 2012; 15:454–459.
6. Alijotas-Reig J, Fernández-Figueras MT, Puig L. Late-Onset Inflammatory Adverse Reactions Related to Soft Tissue Filler Injections. Clin Rev Allergy Immunol. 2013; 45:97–108. [PubMed: 23361999]
7. Lutolf MP, et al. Synthetic matrix metalloproteinase-sensitive hydrogels for the conduction of tissue regeneration: Engineering cell-invasion characteristics. Proc Natl Acad Sci. 2003; 100:5413–5418. [PubMed: 12686696]
8. Galler KM, Aulisa L, Regan KR, D'Souza RN, Hartgerink JD. Self-Assembling Multidomain Peptide Hydrogels: Designed Susceptibility to Enzymatic Cleavage Allows Enhanced Cell Migration and Spreading. J Am Chem Soc. 2010; 132:3217–3223. [PubMed: 20158218]
9. Wang DA, et al. Multifunctional chondroitin sulphate for cartilage tissue-biomaterial integration. Nat Mater. 2007; 6:385–392. [PubMed: 17435762]
10. Kong HJ, Kaigler D, Kim K, Mooney DJ. Controlling rigidity and degradation of alginate hydrogels via molecular weight distribution. Biomacromolecules. 2004; 5:1720–1727. [PubMed: 15360280]
11. Burdick JA, Chung C, Jia X, Randolph MA, Langer R. Controlled Degradation and Mechanical Behavior of Photopolymerized Hyaluronic Acid Networks. Biomacromolecules. 2005; 6:386–391. [PubMed: 15638543]
12. Madden LR, et al. Proangiogenic scaffolds as functional templates for cardiac tissue engineering. Proc Natl Acad Sci. 2010; 107:15211–15216. [PubMed: 20696917]
13. Stachowiak AN, Bershteyn A, Tzatzalos E, Irvine DJ. Bioactive Hydrogels with an Ordered Cellular Structure Combine Interconnected Macroporosity and Robust Mechanical Properties. Adv Mater. 2005; 17:399–403.
14. Gorgieva S, Kokol V. Preparation, characterization, and in vitro enzymatic degradation of chitosan-gelatine hydrogel scaffolds as potential biomaterials. J Biomed Mater Res A. 2012; 100:1655–1667. [PubMed: 22447615]
15. Sokic S, Christenson M, Larson J, Papavasiliou G. In situ generation of cell-laden porous MMP-sensitive PEGDA hydrogels by gelatin leaching. Macromol Biosci. 2014; 14:731–739. [PubMed: 24443002]
16. Hosokawa K, Fujii T, Endo I. Handling of Picoliter Liquid Samples in a Poly(dimethylsiloxane)-Based Microfluidic Device. Anal Chem. 1999; 71:4781–4785.
17. Anna SL, Bontoux N, Stone HA. Formation of dispersions using 'flow focusing' in microchannels. Appl Phys Lett. 2003; 82:364–366.

18. Kawakatsu T, Kikuchi Y, Nakajima M. Regular-sized cell creation in microchannel emulsification by visual microprocessing method. J Am Oil Chem Soc. 1997; 74:317–321.
19. Li CY, Wood DK, Hsu CM, Bhatia SN. DNA-templated assembly of droplet-derived PEG microtissues. Lab Chip. 2011; 11:2967–2975. [PubMed: 21776518]
20. Du Y, Lo E, Ali S, Khademhosseini A. Directed assembly of cell-laden microgels for fabrication of 3D tissue constructs. Proc Natl Acad Sci. 2008; 105:9522–9527. [PubMed: 18599452]
21. Qi H, et al. DNA-directed self-assembly of shape-controlled hydrogels. Nat Commun. 2013; 4
22. Jgamadze D, Liu L, Vogler S, Chu LY, Pautot S. Thermoswitching Microgel Carriers Improve Neuronal Cell Growth and Cell Release for Cell Transplantation. Tissue Eng Part C Methods. 201410.1089/ten.TEC.2013.0752
23. Jgamadze D, et al. Colloids as mobile substrates for the implantation and integration of differentiated neurons into the mammalian brain. PloS One. 2012; 7:e30293. [PubMed: 22295079]
24. Pautot S, Wyart C, Isacoff EY. Colloid-guided assembly of oriented 3D neuronal networks. Nat Methods. 2008; 5:735–740. [PubMed: 18641658]
25. Dunne M, Corrigan OI, Ramtoola Z. Influence of particle size and dissolution conditions on the degradation properties of polylactide-co-glycolide particles. Biomaterials. 2000; 21:1659–1668. [PubMed: 10905407]
26. Chen H, et al. Hydrogel-thickened microemulsion for topical administration of drug molecule at an extremely low concentration. Int J Pharm. 2007; 341:78–84. [PubMed: 17570625]
27. Garstecki P, Fuerstman MJ, Stone HA, Whitesides GM. Formation of droplets and bubbles in a microfluidic T-junction—scaling and mechanism of break-up. Lab Chip. 2006; 6:437–446. [PubMed: 16511628]
28. Conchouso D, Castro D, Khan SA, Foulds IG. Three-dimensional parallelization of microfluidic droplet generators for a litre per hour volume production of single emulsions. Lab Chip. 2014; 14:3011–3020. [PubMed: 24947654]
29. Griffin DR, et al. Hybrid photopatterned enzymatic reaction (HyPER) for in situ cell manipulation. Chembiochem Eur J Chem Biol. 2014; 15:233–242.
30. Schense JC, Hubbell JA. Cross-linking exogenous bifunctional peptides into fibrin gels with factor XIIIa. Bioconjug Chem. 1999; 10:75–81. [PubMed: 9893967]
31. Lutolf MP, Hubbell JA. Synthetic biomaterials as instructive extracellular microenvironments for morphogenesis in tissue engineering. Nat Biotechnol. 2005; 23:47–55. [PubMed: 15637621]
32. Seliktar D, Zisch AH, Lutolf MP, Wrana JL, Hubbell JA. MMP-2 sensitive, VEGF-bearing bioactive hydrogels for promotion of vascular healing. J Biomed Mater Res A. 2004; 68:704–716. [PubMed: 14986325]
33. Chen EJ, Novakofski J, Jenkins WK, O'Brien J, Young's WD. modulus measurements of soft tissues with application to elasticity imaging. IEEE Trans Ultrason Ferroelectr Freq Control. 1996; 43:191–194.
34. Cheng S, Bilston LE. Unconfined compression of white matter. J Biomech. 2007; 40:117–124. [PubMed: 16376349]
35. Parker KJ, Huang SR, Musulin RA, Lerner RM. Tissue response to mechanical vibrations for 'sonoelasticity imaging'. Ultrasound Med Biol. 1990; 16:241–246. [PubMed: 2194336]
36. Samani A, Bishop J, Luginbuhl C, Plewes DB. Measuring the elastic modulus of ex vivo small tissue samples. Phys Med Biol. 2003; 48:2183. [PubMed: 12894978]
37. Yeh WC, et al. Elastic modulus measurements of human liver and correlation with pathology. Ultrasound Med Biol. 2002; 28:467–474. [PubMed: 12049960]
38. Galiano RD, Michaels J, Dobryansky M, Levine JP, Gurtner GC. Quantitative and reproducible murine model of excisional wound healing. Wound Repair Regen Off Publ Wound Heal Soc Eur Tissue Repair Soc. 2004; 12:485–492.
39. Fukano Y, et al. Characterization of an in vitro model for evaluating the interface between skin and percutaneous biomaterials. Wound Repair Regen. 2006; 14:484–491. [PubMed: 16939578]
40. Fukano Y, et al. Epidermal and dermal integration into sphere-templated porous poly(2-hydroxyethyl methacrylate) implants in mice. J Biomed Mater Res A. 2010; 94A:1172–1186. [PubMed: 20694984]

41. Wang HM, et al. Novel Biodegradable Porous Scaffold Applied to Skin Regeneration. PLoS ONE. 2013; 8:e56330. [PubMed: 23762223]
42. Wang X, Ge J, Tredget EE, Wu Y. The mouse excisional wound splinting model, including applications for stem cell transplantation. Nat Protoc. 2013; 8:302–309. [PubMed: 23329003]
43. Ota T, et al. Notch signaling may be involved in the abnormal differentiation of epidermal keratinocytes in psoriasis. Acta Histochem Cytochem. 2014; 47:175–183. [PubMed: 25392571]
44. Bramfeld H, Sabra G, Centis V, Vermette P. Scaffold Vascularization: A Challenge for Three-Dimensional Tissue Engineering. Curr Med Chem. 2010; 17:3944–3967. [PubMed: 20939827]
45. Hollister SJ. Porous scaffold design for tissue engineering. Nat Mater. 2005; 4:518–524. [PubMed: 16003400]
46. Yang S, Leong KF, Du Z, Chua CK. The Design of Scaffolds for Use in Tissue Engineering. Part I Traditional Factors Tissue Eng. 2001; 7:679–689. [PubMed: 11749726]
47. Peters MC, Polverini PJ, Mooney DJ. Engineering vascular networks in porous polymer matrices. J Biomed Mater Res. 2002; 60:668–678. [PubMed: 11948526]
48. Winkler EA, Bell RD, Zlokovic BV. Pericyte-specific expression of PDGF beta receptor in mouse models with normal and deficient PDGF beta receptor signaling. Mol Neurodegener. 2010; 5:32. [PubMed: 20738866]
49. Huang FJ, et al. PERICYTE DEFICIENCIES LEAD TO ABERRANT TUMOR VASCULARIZATON IN THE BRAIN OF THE NG2 NULL MOUSE. Dev Biol. 2010; 344:1035–1046. [PubMed: 20599895]
50. Stratman AN, Malotte KM, Mahan RD, Davis MJ, Davis GE. Pericyte recruitment during vasculogenic tube assembly stimulates endothelial basement membrane matrix formation. Blood. 2009; 114:5091–5101. [PubMed: 19822899]
51. Rustad KC, et al. Enhancement of mesenchymal stem cell angiogenic capacity and stemness by a biomimetic hydrogel scaffold. Biomaterials. 2012; 33:80–90. [PubMed: 21963148]
52. Richardson TP, Peters MC, Ennett AB, Mooney DJ. Polymeric system for dual growth factor delivery. Nat Biotechnol. 2001; 19:1029–1034. [PubMed: 11689847]
53. Sun G, et al. Dextran hydrogel scaffolds enhance angiogenic responses and promote complete skin regeneration during burn wound healing. Proc Natl Acad Sci U S A. 2011; 108:20976–20981. [PubMed: 22171002]
54. Tokatlian T, Cam C, Segura T. Porous Hyaluronic Acid Hydrogels for Localized Nonviral DNA Delivery in a Diabetic Wound Healing Model. Adv Healthc Mater. 201510.1002/adhm.201400783
55. Liang W, et al. Metabolically induced liver inflammation leads to NASH and differs from LPS- or IL-1β-induced chronic inflammation. Lab Invest. 2014; 94:491–502. [PubMed: 24566933]
56. Latger-Cannard V, Besson I, Doco-Lecompte T, Lecompte T. A standardized procedure for quantitation of CD11b on polymorphonuclear neutrophil by flow cytometry: potential application in infectious diseases. Clin Lab Haematol. 2004; 26:177–186. [PubMed: 15163315]
57. Lucas T, et al. Differential Roles of Macrophages in Diverse Phases of Skin Repair. J Immunol. 2010; 184:3964–3977. [PubMed: 20176743]
58. Tokatlian T, Cam C, Segura T. Non-viral DNA delivery from porous hyaluronic acid hydrogels in mice. Biomaterials. 2014; 35:825–835. [PubMed: 24210142]

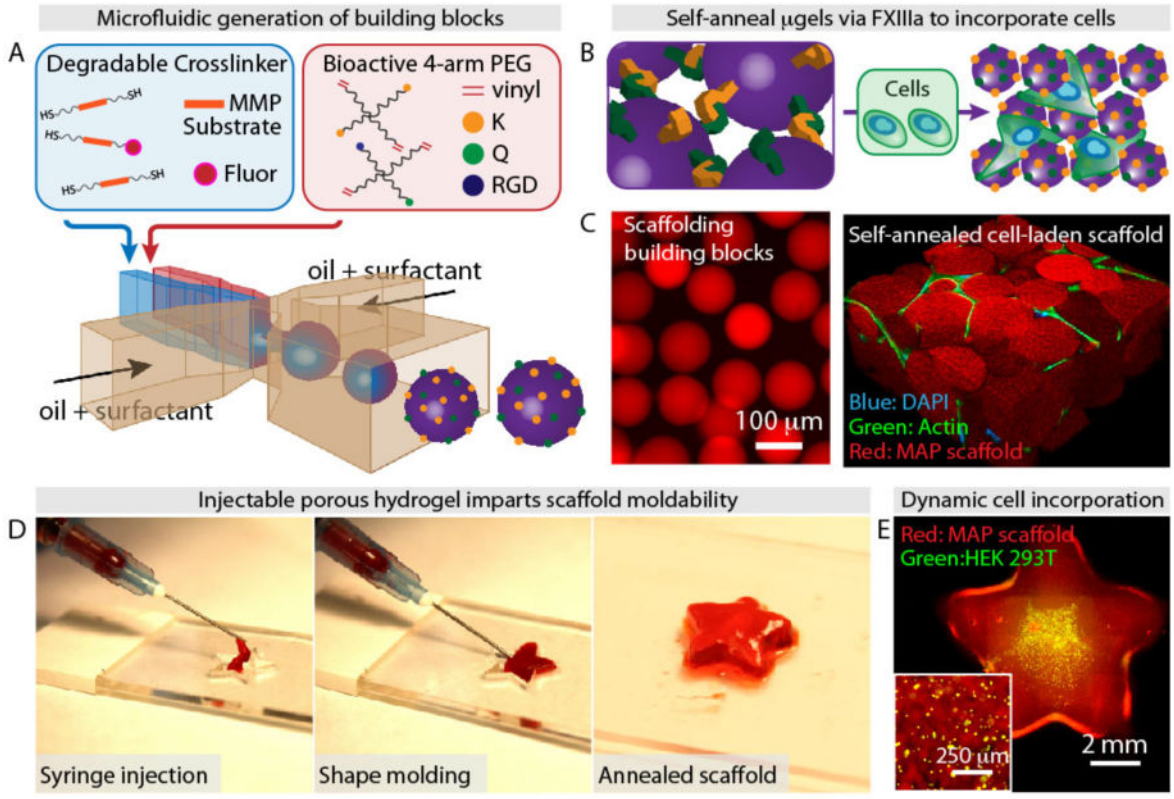

Figure 1.

Microfluidic generation of microsphere hydrogel building blocks for the creation of Microporous Annealed Particle (MAP) scaffolds. A–B: Scheme illustrating μgel formation using a microfluidic water-in-oil emulsion system. A pre-gel and crosslinker solution are segmented into monodisperse droplets followed by in-droplet mixing and crosslinking via Michael-addition. μgels are purified into an aqueous solution and annealed using FXIIIa into a microporous scaffold, either in the presence of cells or as a pure scaffold. C: Fluorescent images showing purified μgel building blocks and a subsequent cell-laden MAP scaffold. D–E: MAP scaffolds are moldable to macro-scale shapes, and can be injected to form complex shapes that are maintained after annealing. A process that can be performed in the presence of live cells.

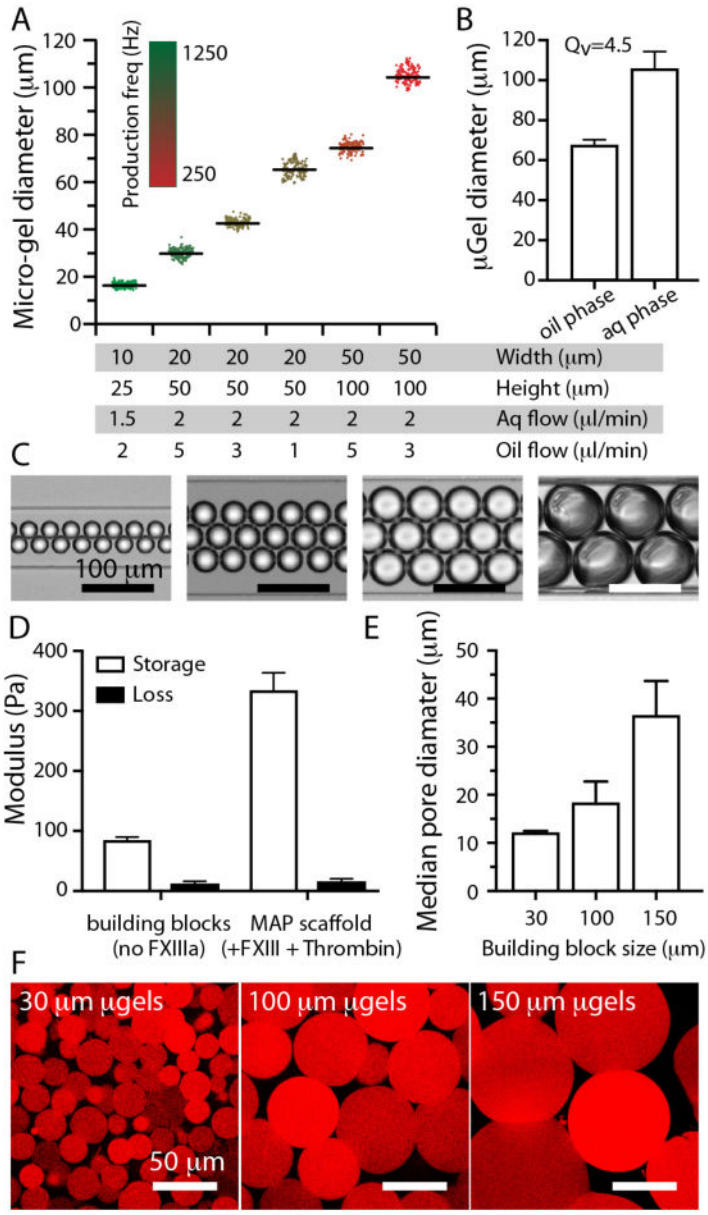

Figure 2.

High precision fabrication of μgel building blocks allows creation of defined MAP scaffolds. A: The operational regime for microfluidic μgel generation has a large dynamic range, spanning almost an order of magnitude in size while maintaining tight control at each condition, with CVs < 6% in all cases. B: Hydrogel building blocks swell in buffer after aqueous extraction from the oil phase. The swelling ratio (Q_v) is predictable and determined by polymer network characteristics. In our chosen formulation, Q_v=4.5. C: Representative images of μgel droplets in flow after generation. D: Rheological characterization of the MAP scaffold. Without the addition of FXIIIa the μgel building blocks display some gel-like characteristics, however the onset of annealing results in significantly increased macro-scale mechanical moduli. E: Different building block sizes allow for deterministic control over resultant micro-porous network characteristics, presented here as median pore sizes +/− SD.

F: Single confocal slices of MAP scaffolds created using different building block sizes. All data presented as average +/−- SD unless otherwise stated. All experiments performed in triplicate.

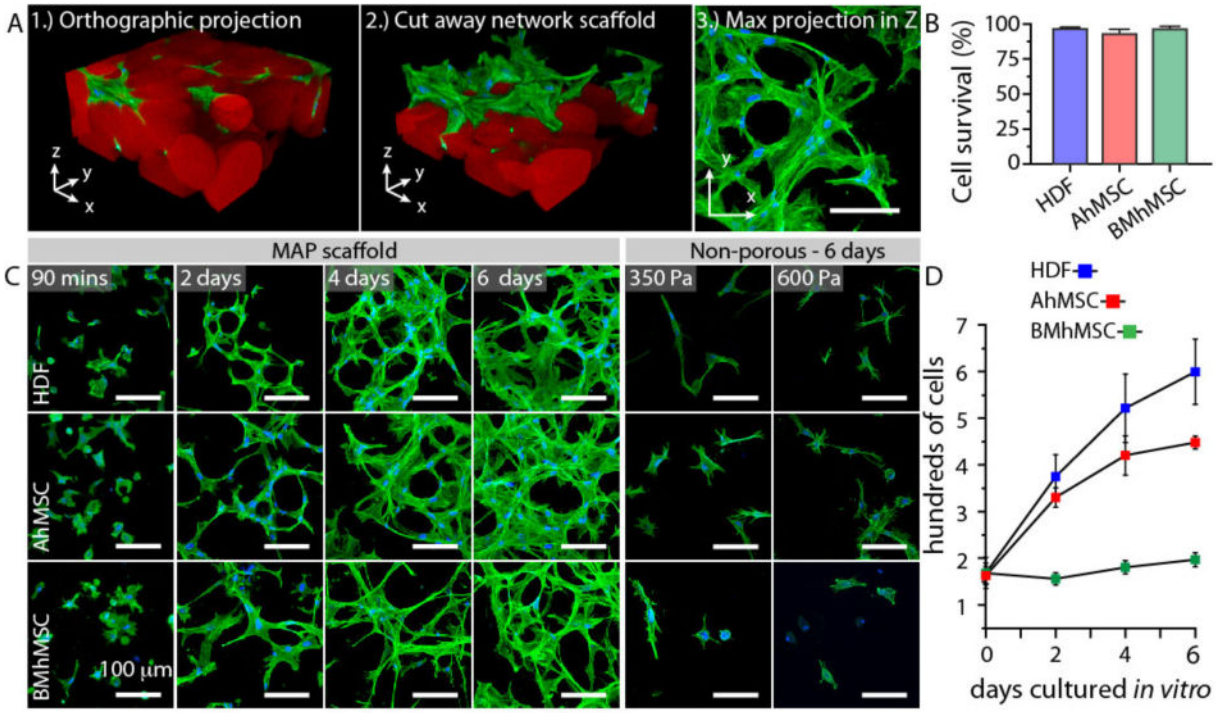

Figure 3.

MAP scaffolds facilitate 3D cellular network formation and proliferation *in vitro*. A: Schematic illustrating how to read images of 3D cell growth and network formation presented in C. B: Cell survival 24 hours post annealing is greater than 93% across three cell lines representing different human tissue types. HDF: Human dermal fibroblasts, AhMSC: Adipose-derived human mesenchymal stem cells, BMhMSC: Bone marrow-derived human mesenchymal stem cells. C: Fluorescent images demonstrating the formation of 3D cellular networks during six days of culture in MAP scaffolds *in vitro* as well as non-porous gels after 6 days. (350 Pa: bulk modulus identical to MAP, 600 Pa: microscale modulus matched to individual μgels) D: Cells proliferate within the MAP scaffold while forming interconnected networks. HDF and AhMSC cells proliferate quickly within the scaffolds with doubling times of ~1.5 and ~2 days, respectively. BMhMSC cells proliferate significantly slower, with a calculated doubling time of ~12 days. These are analogous to previously observed normal growth phenotypes for these lines. All data presented as average +/− SD. All experiments performed in triplicate.

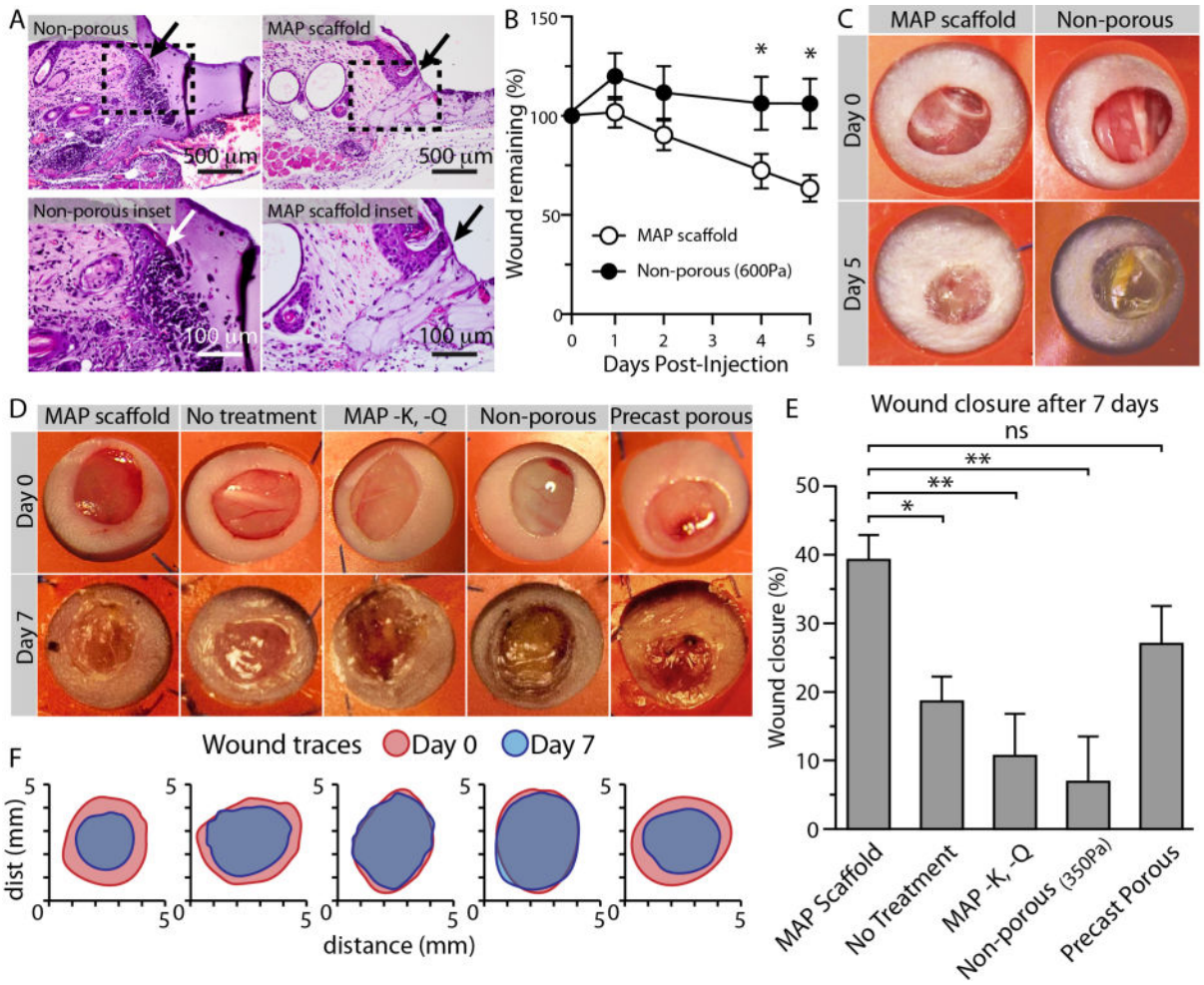

Figure 4.

MAP scaffolds promote fast wound closure in SKH1-Hr^{hr} and Balb/c epidermal mouse models. A: H&E staining of tissue sections indicate seamless integration of the injected MAP scaffold as well as the non-porous control 24 hours post injection in SKH1-Hr^{hr} mice. B: Quantification of wound closure over a 5 day period shows statistically significant wound closure rates for MAP scaffolds when compared to non-porous bilateral controls (N = 5). C: Representative images of would closure during a 5 day *in vivo* wound healing model in SKH1-*Hr*^{hr} mice. D: Representative images of wound closure during 7 day *in vivo* Balb/c experiments. E: Quantification of wound closure data form Balb/c *in vivo* wound healing. After 7 days *in vivo*, the MAP scaffolds promote significantly faster wound healing than the no treatment control, the non-porous PEG gel, and the MAP gels lacking the K and Q peptides. Porous gels created *ex vivo* to precisely match the wound shape using the canonical, porogen-based, casting method showed appreciable wound healing rates, comparable to the MAP scaffolds, but lacking injectability (N≥5). F: Traces of wound bed closure during 7 days *in vivo* for each treatment category. All data are presented as average +/− SEM. Statistical significance performed using standard two-tailed t-test (*: $p<0.05$; **$p<0.01$).

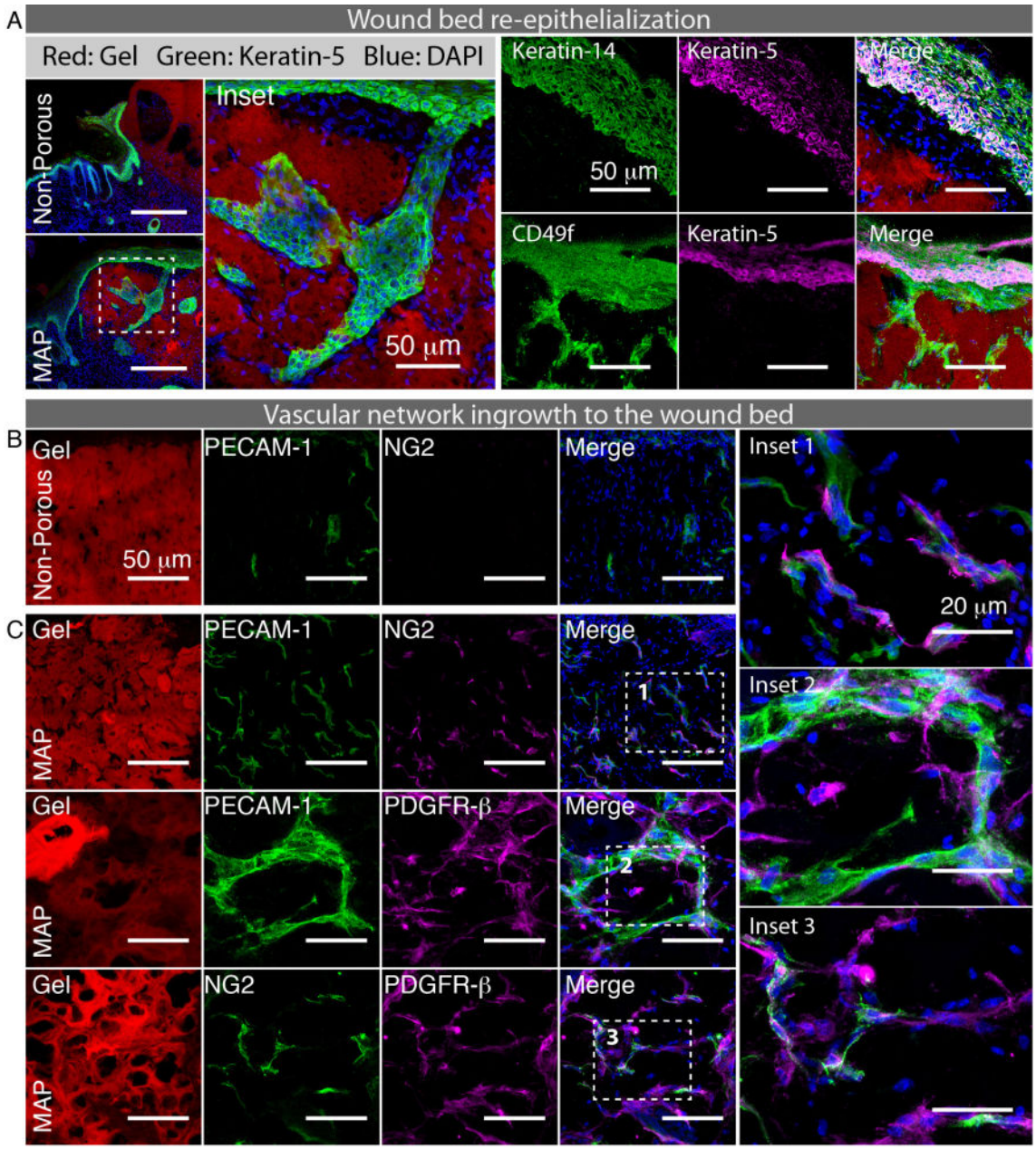

Figure 5.

MAP scaffolds allow for faster tissue regeneration compared to non-porous controls *in vivo*. A: Matching wound closure data (Figure 4), the MAP scaffolds also allow for significant re-epithelialization 5 days post injection. By comparison, the non-porous constructs show very little to no re-epithelialization by day 5. Importantly, in addition to stratified expression of keratin-5, keratin-14, and CD49f above the gel, we also observe large-scale tissue structures within the construct. Keratin-5 staining of the basement epithelial layer outline developing hair follicles and sebaceous glands within the MAP scaffold after 5 days. Non-porous controls are devoid of similar complex multicellular structures. B–C?: MAP scaffolds contain large networks of cells staining positive for the endothelial marker, PECAM-1,

juxtapositioned with cells expressing NG2 and PDGFR-β (a pericyte phenotype), indicative of developing vasculature.

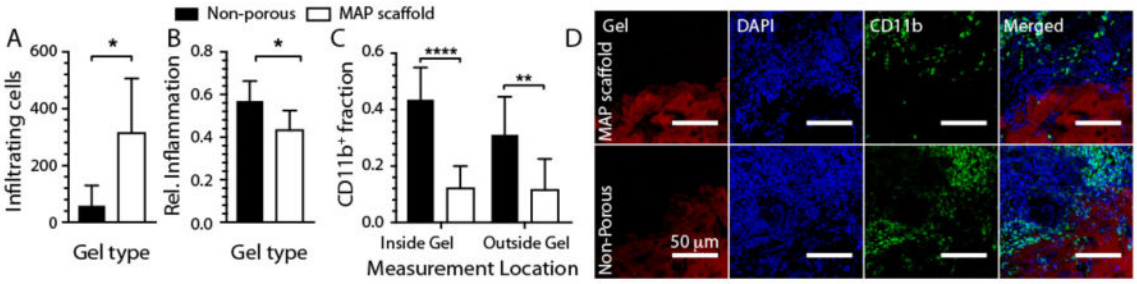

Figure 6.

MAP scaffolds elicit a significantly lower immune response than non-porous hydrogels *in vivo.* A: Quantification of both total cellular infiltration into the constructs and immune response in the surrounding tissue 24 hours post injection. Inflammation is measured using a paired test for each mouse, where the fraction is the number of inflammatory cells for each construct relative to its bilateral control. C: Quantification of immune response 5 days after injection, as measured by the fraction of total cells expressing CD11b. MAP scaffolds elicit a significantly lower response of $CD11b^{+}$ cells as compared to non-porous controls, both inside the construct and in the surrounding tissue. D: Representative images of tissue sections from 5 days after injection for MAP scaffolds and non-porous controls. All data presented as average +/− SD. Statistical significance performed using standard two-tailed t-test (*: $p<0.05$; **$p<0.01$; ****$p<0.001$).